RSC Advances

PAPER

View Article Online
View Journal | View Issue

Cite this: *RSC Adv.*, 2026, **16**, 3276

Sequential electroporation and biomimetic mineralization on an *E. coli* biotemplate: green synthesis of functional porous hollow calcium phosphate capsules

Wen Jiang,†[a] Fengwu Zhang,†[bc] Mengyao Bian,[a] Jingxuan Han[a] and Changyu Shao *[a]

Received 30th August 2025
Accepted 30th December 2025

DOI: 10.1039/d5ra06501a

rsc.li/rsc-advances

By leveraging *E. coli* as a biotemplate combined with electroporation and biomimetic mineralization, we developed biosafe porous hollow calcium phosphate capsules (PHCPCs) with a well-defined structure. This approach enables the precise and tunable encapsulation of various cargoes, such as therapeutic drugs and single/multiple metal oxide nanoparticles.

The hollow structured materials, particularly in the case of calcium phosphate (CaP)-based microspheres, have garnered a lot of scientific interest owing to their compelling advantages for a range of applications.[1,2] They have a huge hollow interior volume and a high specific surface area due to their distinctive three-dimensional construction. These structural characteristics offer several fundamental advantages: they significantly enhance surface adsorption and reaction activity, enabling the incorporation of higher payloads (*e.g.*, therapeutic agents or catalysts), and facilitate better control over release kinetics.[3,4] Furthermore, CaP materials inherently possess valuable properties such as bioactivity, biodegradability, biocompatibility, and osteoconductivity.[5,6] Consequently, hollow CaP structures have great potential, particularly in demanding domains such as bone tissue engineering and targeted drug delivery.[7,8] This strong potential underscores the critical need for developing synthesis techniques capable of precise control over the composition and architecture of these materials.

Numerous synthetic approaches have been developed to fabricate hollow porous structured CaP microspheres, primarily relying on templating or assisting agents.[9] Common strategies encompass the assembly of hydroxyapatite (HAP) using amino acids, surfactants, polymers, DNA, proteins, or chelators.[10–12] Alternative methods include solvothermal synthesis and microwave/sonication–surfactant combination techniques, utilizing chelate reagents or creatine phosphate as an organic phosphorus source.[13,14] However, these established routes frequently require substantial amounts of auxiliary reagents and templates, expensive phosphorus sources, extended reaction durations (*e.g.*, several hours for hydrothermal $CaCO_3$ template conversion), and potentially hazardous organic solvents, thereby imposing practical and environmental constraints. By contrast, biomimetic synthesis inspired by biomineralization processes, offers a promising alternative. This approach employs multicomponent organic–inorganic systems where organic components, particularly organism-based templates, facilitate inorganic mineral deposition.[15] Biotemplates obtained from unicellular organisms offer significant benefits compared to synthetic polymers, macromolecules, or inorganic particles, such as unique microstructures, remarkable uniformity in size and morphology, and intrinsic surface functionality. Templated synthesis using these biological platforms has thus emerged as an efficient and convenient method for generating well-defined, porous hollow calcium phosphate capsules (PHCPCs), overcoming numerous limitations of traditional synthesis.

Gram negative bacteria, *Escherichia coli* (*E. coli*), is extensively utilized as a model organism in biomedical and biotechnological research,[16] primarily due to its rapid proliferation and low cost. The cell wall, primarily consisting of lipopolysaccharide (LPS) and peptidoglycan (PG), contains numerous negatively charged groups such as carboxylates.[17] These groups electrostatically attract multivalent metal cations (*e.g.*, Ca^{2+}, Fe^{3+}), facilitating their deposition and initiating mineral nucleation on the cellular surface.[18] In addition, applying high-voltage electrical pulses using electroporation technique can create instantaneous pores (10–100 nm) on the cell membrane, which allow nanoparticles (NPs), proteins, and other macromolecules to effectively enter the cells.[19,20]

[a]*Stomatology Hospital, School of Stomatology, Zhejiang University School of Medicine, Clinical Research Center for Oral Diseases of Zhejiang Province, Key Laboratory of Oral Biomedical Research of Zhejiang Province, Cancer Center of Zhejiang University, Hangzhou, 310016, China. E-mail: shaocy@zju.edu.cn*

[b]*Cancer Institute, The Second Affiliated Hospital Zhejiang University School of Medicine, Hangzhou, 310009, China*

[c]*Institute of Translational Medicine Zhejiang University School of Medicine, Hangzhou, 310029, China*

† Wen Jiang and Fengwu Zhang contributed equally to this work.

Consequently, different types of NP-loaded PHCPCs can be readily produced *via E. coli* mineralization, followed by calcination to remove the biotemplate. Herein, we successfully fabricated single- and multiple-type metal oxide nanoparticle-loaded PHCPCs *via* sequential electroporation, mineralization, and calcination. We further validated the low cytotoxicity of PHCPCs toward normal cells and the therapeutic potency of doxorubicin-loaded PHCPCs against tumor cells. Extending this strategy enables production of PHCPCs loaded with various substances, including inorganic nanoparticles and organic molecules.

The *E. coli* was selected as the model organism and mineralized in a mineralization system. Following a 3 day mineralization period, elemental analysis indicates the formation of a dense calcium phosphate mineral shell (Fig. S1). In comparison to the pristine group, the presence of calcium in the mineralized group is notable, as the mapping image reveals a uniform distribution of calcium on the surface along with a distinct outline under observation of scanning electron microscopy (SEM) and scanning transmission electron microscopy (STEM) (Fig. 1a–f and j). To determine the mineralization rate, the *E. coli* were further labelled with FITC-D-Lys during the cultivation stage, while the HAP minerals were labelled with calcein deep red at the end of the mineralization. Subsequently, the confocal laser scanning microscope (CLSM) was performed, and the fluorescence image was collected. In this image, the red indicates the mineralized *E. coli*, whereas the green indicates all of the observed *E. coli*. Accordingly, the mineralization rate could be calculated, and the figure is around 57%.

To determine the precise phase of the CaP mineral, the surface deposit on *E. coli* was analyzed by HRTEM, FTIR, and XPS. The crystallographic plane (200) with an interplanar spacing of 0.40 nm was determined, and this value corresponds with that of the HAP crystals (Fig. 1i). In addition, the FTIR spectra of mineralized *E. coli* exhibit two characteristic peaks at 567 cm^{-1} and 607 cm^{-1}, which correspond to the asymmetric bending vibration of the P–O band in HAP (Fig. 1k). Furthermore, in the XPS spectra of mineralized *E. coli*, Ca $2p_{3/2}$, Ca $2p_{1/2}$ and P 2p peaks were detected at 347.2 eV, 350.8 eV and 133.2 eV, respectively; these values are consistent with those of HAP. In contrast, no calcium was detected in pristine *E. coli* (Fig. 1l and S2). These results collectively demonstrated that the synthesized CaP mineral predominantly exists in the form of HAP crystals, and showed that this straightforward mineralisation approach can effectively promote the formation of a mineral shell on the surface of *E. coli*.

After mineralization of *E. coli*, a layer of HAP minerals formed on its surface. The biotemplate of *E. coli*, which is composed of organic matter, was then subjected to calcination to remove the organic components, resulting in the production

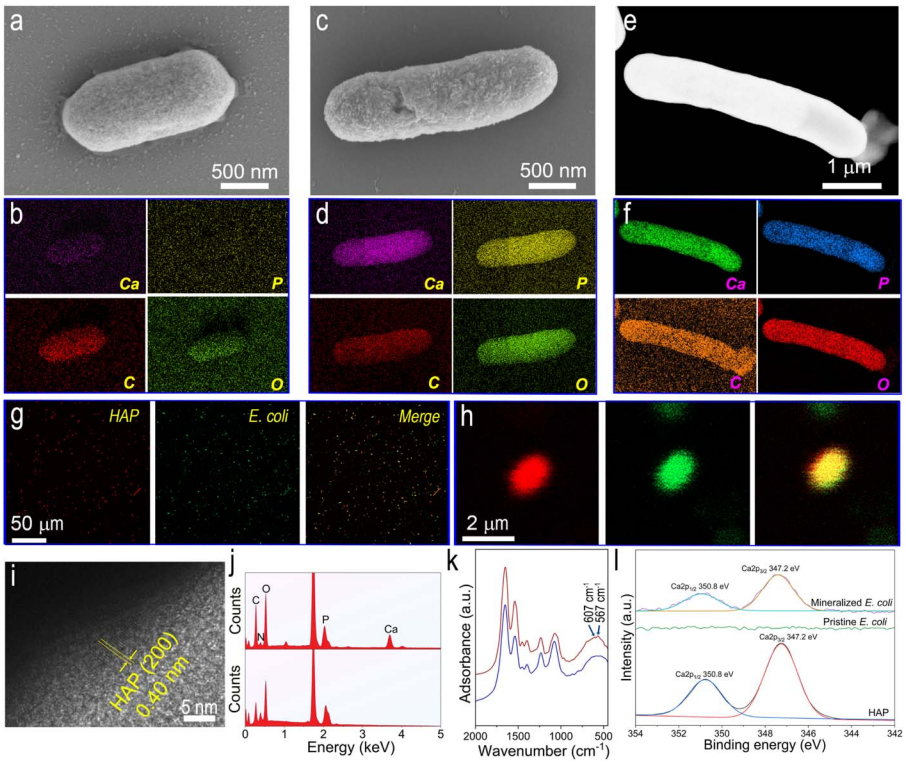

Fig. 1 (a) and (b), and (c) and (d) SEM image of pristine and mineralized *E. coli* and their corresponding elemental mapping, respectively. (e) and (f) STEM image of mineralized *E. coli* and their corresponding elemental mapping. (g) and (h) CLSM images of mineralized *E. coli* at low and high magnification. The HAP labelled with calcein deep red emits red fluorescence, while the *E. coli* labelled with FITC emits green fluorescence. (i) HRTEM image of the mineral that forms on the mineralized *E. coli*. (j) The elemental analysis of the pristine *E. coli* (bottom) and mineralized *E. coli* (top). (k) and (l) FTIR and XPS spectra of the pristine *E. coli* and mineralized *E. coli*. The dark blue and red lines in the FTIR spectra represent pristine and mineralized *E. coli*, respectively.

of PHCPCs, with lengths of 2.61 ± 0.66 μm and widths of 0.88 ± 0.13 μm (Fig. S3). The TGA curve revealed the entire mass loss *versus* temperature profile. The initial mass loss observed up to 100 °C corresponds to the removal of water from the HAP-coated cells and accounts for approximately 5.7% of the total mass. In the second stage, mass loss occurs between approximately 200 °C and 600 °C. The corresponding differential thermogravimetric (DTG) curve shows five distinct peaks, which are attributed to the sequential decomposition and combustion of organic components. Beyond 600 °C, the mass stabilizes as no further significant mass loss occurs. Therefore, calcination was performed at 600 °C to ensure complete removal of organic components, yielding the final PHCPCs.

The prepared PHCPC was collected and observed under SEM and transmission electron microscopy (TEM; Fig. 2b and c). The PHCPC retains the characteristic rod-like morphology of the *E. coli* biotemplate. Its surface appears smooth and dense under electron microscopy, suggesting complete coverage by consolidated HAP minerals during mineralization and optimal template removal during calcination at 600 °C. In addition, the hollow structure and surface pores (indicated by yellow arrows in Fig. 2b and c) were observed, which enhance mass transfer into and out of the PHCPC material. Furthermore, powder X-ray diffraction (PXRD) analysis identified a biphasic system in PHCPC. One of the phases was indexed to HAP (Joint Committee on Powder Diffraction Standards (JCPDS) or Powder Diffraction File (PDF) card: 00-09-0432), with characteristic diffraction at: 18.7° (110), 23.2° (111), 24.9° (201), and 28.8° (210). Another phase, calcium pyrophosphate (CPP, JCPDS/PDF: 00-09-0346), was detected at: 26.5° (200), 26.8° (201), 27.6° (202), and 29.5° (008). The HAP derived from mineralization and the pyrophosphate that forms CPP may be attributed to the decomposition of phosphorus-containing organic molecules, such as phospholipids. Furthermore, the BET surface area of the PHCPCs, reflecting the external surface and accessible porosity of the mineral shell, was approximately 10.6 $m^2 g^{-1}$, as calculated from the N_2 adsorption isotherms (Fig. 2e). The BJH analysis of the adsorption branch yielded an average pore diameter of 22.3 nm (Fig. 2f), indicating a mesoporous structure within the shell.

The synthesis of core–shell inorganic materials typically involves a multi-step chemical reaction process, and the core is usually a monocomponent, hence constraining their functional applications. To prepare multicomponent cores, we developed a new method using electroporation to create transient pores in the membranes of viable *E. coli* cells. The formation of these pores is driven by the progressive alignment of water and lipid dipoles under the electric field gradients at the membrane interface,[21,22] which enabled the entry of nanoparticles whose diameters ranged from a few nanometers to 100 nm. Accordingly, metal oxides such as TiO_2 and ZnO were used as model nanoparticles to validate electroporation-assisted cellular entry. These nanoparticles were first examined by TEM to assess morphology and size, revealing diameters of 13.0 ± 0.5 nm for TiO_2 and 17.8 ± 0.9 nm for ZnO (Fig. 3a and b). PXRD was further employed to determine crystallographic phase, where diffraction peaks at $2\theta = 25.3°$ corresponded to the (101) plane of anatase TiO_2, while peaks at 31.8°, 34.5°, and 36.3° indexed to the (100), (002), and (101) planes of zincite ZnO, respectively. Additionally, crystallite sizes (D) of TiO_2 and ZnO were calculated using the Scherrer equation, resulting in $D = 13.2$ nm for TiO_2 (from the 25.3° 2θ peak) and $D = 17.9$ nm for ZnO (from the 36.3° 2θ peak), which aligns with the TEM results (Fig. 3i).

Initially, TiO_2 alone or a TiO_2/ZnO mixture was introduced into *E. coli* cell suspensions, with electroporation facilitating nanoparticle internalization. Following mineralization and calcination, both the single-component TiO_2 and the multi-component (TiO_2 and ZnO) were detected within the PHCPCs. The surface porosity of metal-oxide-loaded PHCPCs was evident (marked with yellow arrows), facilitating the transport of the substance (Fig. 3b and f). The interior of the metal-oxide-loaded PHCPCs was examined through the fractured sample, followed by elemental analysis. The mineral shell thickness of TiO_2-loaded PHCPCs, measured *via* SEM, ranged from 45 to 70 nm

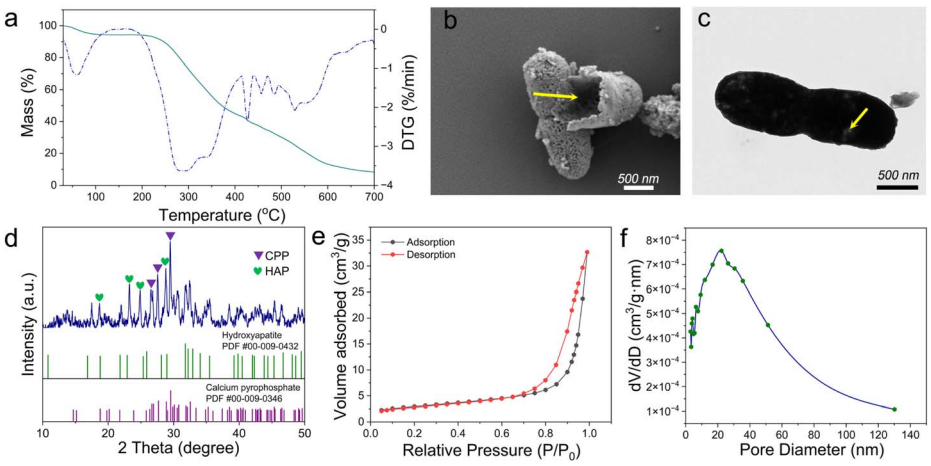

Fig. 2 (a) The TGA of PHCPCs. (b) SEM and (c) TEM image of PHCPC. (d) XRD analysis of PHCPCs. (e) N_2 adsorption–desorption isotherm and (f) pore diameter distributions of PHCPCs.

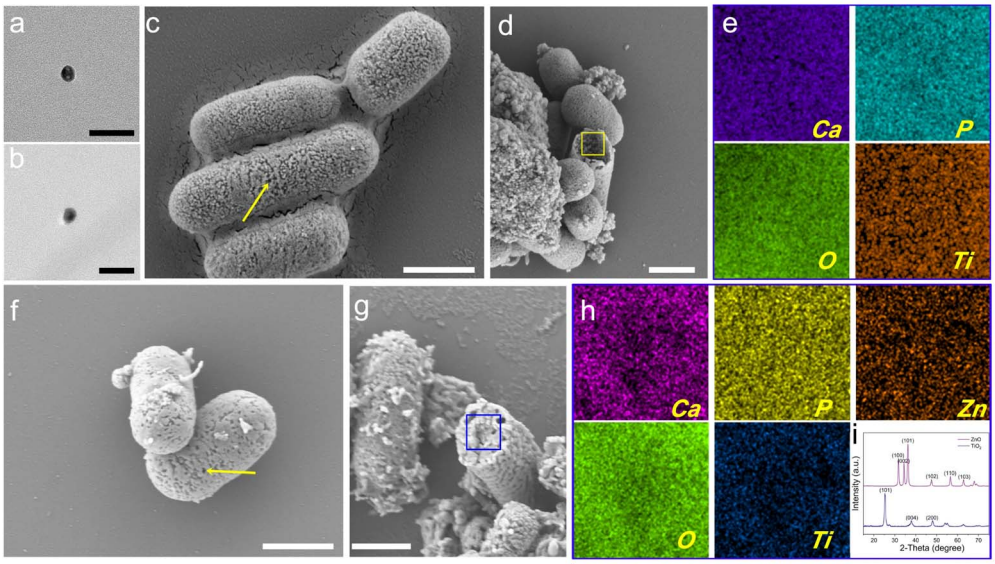

Fig. 3 (a) and (b) TEM images of TiO_2 and ZnO nanoparticles. (c) and (d) SEM images of intact and chapped TO_2 nanoparticle-loaded PHCPCs. (e) The elemental mapping of the area indicated in the yellow box in (b) reveals the Ca and P originating from CaP mineral, and Ti sourced from TiO_2. (f) and (g) SEM images of intact and chapped PHCPCs loaded with both TiO_2 and ZnO nanoparticles. (h) The elemental mapping of the region in the blue box in (g) demonstrates that Ca and P are derived from CaP mineral, Ti from TiO_2, and Zn from ZnO. (i) XRD spectra of TiO_2 and ZnO. Scale bar: (a) and (b) 50 nm; (c), (d), (f) and (g) 1 μm.

(Fig. 3d). The TiO_2 nanoparticles were distinctly visible within the PHCPCs, and elemental mapping corroborated this, indicating that Ca and P originated from the mineral, while Ti was derived from TiO_2 (Fig. 3d and e). In addition, TiO_2 and ZnO can simultaneously penetrate PHCPCs and occupy their internal spaces, which was corroborated by the elemental mapping (Fig. 3g and h). Through these two cases of the metal-oxide-loaded PHCPCs, we developed a new approach for synthesizing diverse core–shell materials, extendable to other inorganic nanoparticle systems.

The *in vitro* cytotoxicity tests of the PHCPCs were performed using MEF cells that isolated from E13.5 embryos of C57BL/6 mice. MEF cells exposed to graded concentrations of PHCPCs (25–100 μg mL^{-1}) showed no observable changes in morphology or density under Bright-field microscopy (Fig. 4a–d). Consistent with these observations, the CCK-8 assay revealed no significant difference in viability at 12 h between PHCPC-treated cells and untreated controls across all concentrations tested (Fig. 4i). When MEF and PHCPCs were co-cultured for 24 h and 48 h, MEF cell proliferation exhibited a modest increase. These results suggest that PHCPCs, at the tested concentrations, exhibited no cytotoxicity, indicating its potential as a biocompatible material.

Additionally, DOX-loaded PHCPCs (DLC: ~285 mg g^{-1}) were prepared and their anti-tumor activity evaluated. When A549 cells (purchased from American Type Culture Collection, USA) were co-cultured with DOX-loaded PHCPCs (25–100 μg mL^{-1}), CLSM and optical images revealed a concentration-dependent reduction in cell density (Fig. 4e–h). During the first 12 h of treatment, DOX-loaded PHCPCs exhibited strong anti-tumor activity against A549 cells at all tested concentrations, with efficacy increasing in a concentration-dependent manner. Cell viability further decreased after 48 h of co-culture. For instance, at 100 μg mL^{-1} DOX-loaded PHCPCs, viability declined from 64.4% to 30.0%. These findings therefore further demonstrate the potential of PHCPCs for drug delivery in disease treatment.

In summary, this work establishes a new *E. coli*-templated biomimetic strategy for synthesising PHCPCs, overcoming the critical limitations of conventional methods. By integrating sequential electroporation and mineralization, we achieved the efficient loading of diverse NPs (single- and multi-type metal

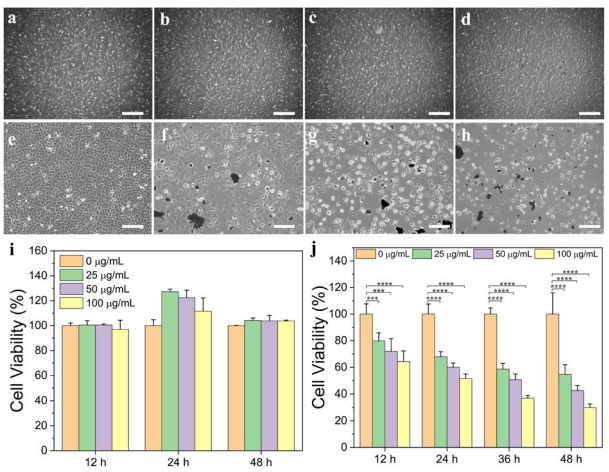

Fig. 4 Optical images of MEF co-cultured with different concentrations of PHCPC: (a) 0 μg mL^{-1}, (b) 25 μg mL^{-1}, (c) 50 μg mL^{-1}, and (d) 100 μg mL^{-1}. Optical images of A549 co-cultured with different concentrations of DOX-loaded PHCPC: (e) 0 μg mL^{-1}, (f) 25 μg mL^{-1}, (g) 50 μg mL^{-1}, and (h) 100 μg mL^{-1}. Scale bar: 200 μm. (i) and (j) CCK8 tests of MEF and A549 cells to detect cell viability.

oxides) into hollow capsules. This is a dual-function biotemplate strategy has not been reported in CaP synthesis before. This approach opens up a new avenue in hollow mineral synthesis, eliminating toxic reagents and multi-step reactions. Future work will focus on *in vivo* targeting efficiency, stimuli-responsive shell engineering, and expanding to macromolecular cargoes (*e.g.*, siRNA) for theranostic applications.

Author contributions

Wen Jiang: data curation, formal analysis, investigation, methodology, writing – original draft. Fengwu Zhang: data curation, formal analysis, investigation, methodology. Mengyao Bian: data curation, formal analysis. Jingxuan Han: data curation. Changyu Shao: conceptualization, data curation, formal analysis, funding acquisition, investigation, project administration, visualization, writing – review & editing.

Conflicts of interest

There are no conflicts to declare.

Ethical statement

All animal procedures were performed in accordance with the Guidelines for Care and Use of Laboratory Animals of Zhejiang University and experiments were approved by the Animal Ethics Committee of the Second Affiliated Hospital of Zhejiang University School of Medicine.

Data availability

The data supporting this article have been included as part of the supplementary information (SI). Supplementary information: experimental methods and Fig. S1–S3. See DOI: https://doi.org/10.1039/d5ra06501a.

Acknowledgements

We acknowledge X. Zheng and D. Qi from the Analysis Center of Agriculture, Life and Environment Sciences, Zhejiang University, for their technical assistance with SEM. This project was funded by the National Science Foundation for Young Scientists of China (Grant no. 22205202) and the Zhejiang Provincial Natural Science Foundation of China (Grant no. LTGY24B010001).

Notes and references

1 X. Wang, J. Feng, Y. Bai, Q. Zhang and Y. Yin, *Chem. Rev.*, 2016, **116**, 10983.
2 R. Chen, J. Shi, B. Zhu, L. Zhang and S. Cao, *Microporous Mesoporous Mater.*, 2020, **306**, 110447.
3 Y. Li and J. Shi, *Adv. Mater.*, 2014, **26**, 3176.
4 X. Cao, G. Wang, K. Wang, L. Guo, Y. Cao, X. Cao and Y. Yang, *Nanoscale Res. Lett.*, 2020, **15**, 69.
5 R. Z. LeGeros, *Clin. Orthop. Relat. Res.*, 2002, **395**, 81.
6 M. Tavoni, M. Dapporto, A. Tampieri and S. Sprio, *J. Compos. Sci.*, 2021, **5**, 227.
7 H. Yang, H. Gao and Y. Wang, *J. Microencapsulation*, 2016, **33**, 421.
8 S. Safi, F. Karimzadeh and S. Labbaf, *Mater. Sci. Eng., C*, 2018, **92**, 712.
9 H. Chen and S. Leng, *Ceram. Int.*, 2015, **41**, 2209.
10 D. Hagmeyer, K. Ganesan, J. Ruesing, D. Schunk, C. Mayer, A. Dey, N. A. J. M. Sommerdijk and M. Epple, *J. Mater. Chem.*, 2011, **21**, 9219.
11 H. Yang, L. Hao, N. Zhao, C. Du and Y. Wang, *CrystEngComm*, 2013, **15**, 5760.
12 C. Qi, Y. J. Zhu, B. Q. Lu, X. Y. Zhao, J. Zhao and F. Chen, *J. Mater. Chem.*, 2012, **22**, 22642.
13 M. G. Ma and J. F. Zhu, *Eur. J. Inorg. Chem.*, 2009, **2009**, 5522.
14 G. J. Ding, Y. J. Zhu, C. Qi, B. Q. Lu, J. Wu and F. Chen, *J. Colloid Interface Sci.*, 2015, **443**, 72.
15 M. Huang and Y. Wang, *J. Mater. Chem.*, 2012, **22**, 626.
16 B. Franco and N. I. Vargas-Maya, in *Escherichia coli - Recent Advances on Physiology, Pathogenesis and Biotechnological Applications*, ed. A. Samie, IntechOpen, Rijeka, 2017, ch. 13, p. 253.
17 C. Weidenmaier and A. Peschel, *Nat. Rev. Microbiol.*, 2008, **6**, 276.
18 L. A. Clifton, M. W. A. Skoda, A. P. Le Brun, F. Ciesielski, I. Kuzmenko, S. A. Holt and J. H. Lakey, *Langmuir*, 2015, **31**, 404.
19 W. J. Dower, J. F. Miller and C. W. Ragsdale, *Nucleic Acids Res.*, 1988, **16**, 6127.
20 Y. Cao, E. Ma, S. Cestellos-Blanco, B. Zhang, R. Qiu, Y. Su, J. A. Doudna and P. Yang, *Proc. Natl. Acad. Sci. U. S. A.*, 2019, **116**, 7899.
21 D. P. Tieleman, *BMC Biochem.*, 2004, **5**, 10.
22 P. T. Vernier and M. J. Ziegler, *J. Phys. Chem. B*, 2007, **111**, 12993.